Full Paper

Wiley Online Library

ELECTROANALYSIS

DOI: 10.1002/elan.202060294

Carbon Encapsulated Ternary Mn–Ni–Co Oxide Nanoparticles as Electrode Materials for Energy Storage Applications

Tarekegn Heliso Dolla,[a, b] Isiaka A. Lawal,[b] Dave G. Billing,[c] Karin Pruessner,[d] and Patrick Ndungu*[b]

Celebrating the 65th Birthday of Prof Emmanuel I. Iwuoha: Electrochemistry in Africa

Abstract: Ternary transition metal oxides are promising advanced materials for use as electrode components in electrochemical energy storage systems. However, low electronic/ionic conductivity hinder practical applications. In this study, ternary Mn–Ni–Co oxide nanoparticles were encapsulated in carbon nanosheets, to improve the electrical conductivity and surface area. When tested as supercapacitor electrodes, the materials exhibited specific capacity of 91.2 $mAh\,g^{-1}$ at a current density of 1 $A\,g^{-1}$ in 2 M KOH. Moreover, after 3000 cycles the composite achieved a specific capacity of 74.6 $mAh\,g^{-1}$ at a current density of 6 $A\,g^{-1}$ and high capacitance retention of 96.4 %.

Keywords: Ternary transition metal oxides · carbon coating · supercapacitors · battery like storage · *Current affiliation:*

1 Introduction

Currently, global demand for clean, renewable, and sustainable energy sources has prompted the need for efficient energy conversion and storage devices [1–4]. This is mainly due to the need to keep pace with the growing global economy, the rapid exhaustion of conventional fuel sources, and address the continual environmental issues from the use of fossil fuels [5,6]. In this regard, electrochemical energy storage technologies are considered as one of the most effective and easiest to apply in many areas of energy conversion or storage, which includes batteries, fuel cells, and supercapacitors [7]. In terms of energy storage, supercapacitors are an area of rapid and growing research interest globally.

Supercapacitors, are systems that utilize electrochemical processes to store and discharge energy, and although they are used in conjunction with rechargeable battery systems, they may one day replace the currently dominant rechargeable battery technology [3,7,8]. They have several advantageous features when compared to batteries, such as, longer lifecycle, environmentally friendly, high power density, excellent shelf life, faster charge/discharge processes, and highly efficient [8,9]. Supercapacitors are classified as electrochemical double layer capacitors (EDLCs), pseudo-capacitors, or hybrid electrochemical capacitors based on the energy storage mechanism [10]. EDLCs operate based on surface charge storage mechanism at the electrode-electrolyte interface, while in pseudocapacitors charge is stored via reversible redox reactions at the surface of electrode materials, and hybrid systems use electrode materials that display both battery-type and capacitive-type behavior [11]. Battery-type electrode materials with a hybrid energy storage mechanism that can overcome the current limitations have recently attracted growing research interest [12]. The electrochemical signature of the battery-type materials includes obvious redox peaks with a separated potential in the CV curve and a nonlinear GCD curve with the presence of a distinct plateau, which differs from that of EDLC-based or pseudocapacitive materials [13].

Recently, tremendous effort has been made in the search for high-performance electrode materials that can be used in supercapacitor systems. The main electrode materials being investigated include carbon-based materials [14], transition metal oxides or hydroxides [15] and conducting polymers [16]. Among these, transition metal oxides are widely explored due to their high-rate capability and exhibit electrochemical characteristics of bat-

[a] T. Heliso Dolla
Department of Chemistry, Wolaita Sodo University, Wolaita Sodo, Ethiopia
[b] T. Heliso Dolla, I. A. Lawal, P. Ndungu
Energy, Sensors and Multifunctional Nanomaterials Research Group,
Department of Chemical Sciences,
University of Johannesburg, Doornfontein Campus, Johannesburg, South Africa
E-mail: pndungu@uj.ac.za
[c] D. G. Billing
DST-NRF Centre of Excellence in Strong Materials and Molecular Sciences Institute,
School of Chemistry,
University of the Witwatersrand, Johannesburg, South Africa
[d] K. Pruessner
School of Chemistry and Physics,
University of KwaZulu-Natal, Durban, South Africa

Supporting information for this article is available on the WWW under https://doi.org/10.1002/elan.202060294

tery-like electrodes [17]. Transition-metal oxides, with multi-metal components, are observed to display remarkable electrochemical performance [18–20] by delivering richer surface redox reactions and displaying enhanced electrical conductivity compared to the simple transition metal oxides [21,22]. In this regard, ternary spinel Mn–Ni–Co oxides have been investigated as attractive electrode materials with improved super-capacitive properties [23–27]. The improvement in the electrochemical performance is attributed to the synergetic effects of the multiple oxidation states and high electrical conductivity of the mixed metal oxides, endowing them superior performance than that of single and binary transition metal oxides [18,21].

However, due to their poor electrical conductivity and sluggish ion diffusion, most mixed transition metal oxides are observed to show lower electrochemical performance than expected further hindering its practical applications. One promising way to address these limitations is to fabricate a hybrid structure composed of the mixed transition metal oxides and carbon materials [28]. The carbon materials serve as a substrate to support the metal oxides and maintain structural integrity of the hybrid materials [29–31]. Despite the numerous research reports on the preparation of hybrid nanostructures, developing simple methods to manufacture such nanostructures remains a challenging area of research. Recently, Fu *et al.* [32] have reported spinel $MnCo_2O_4$/C hybrid nanostructures consisting of $MnCo_2O_4$ nanoparticles dispersed uniformly on a porous carbon nanosheets, prepared by using glucose and NaCl as a carbon source and template, respectively. Here the NaCl plays an important role in the formation of 2D nanosheets. Similar method was reported by Wen *et al.* [33], in which Co_3O_4 nanoparticles were homogeneously encapsulated in an ultrathin porous graphitic carbon. This synthetic method is incredibly attractive due to its low cost, simplicity, and the possibility of extending it to multicomponent transition metal oxides.

Herein, we report carbon coated ternary Mn–Ni–Co oxide nanoparticle based hybrid nanostructure employing the strategy reported by Fu *et al.* [32] and modifying the citrate sol-gel method reported in our previous study [34]. Making use of NaCl as a template, Mn–Ni–Co–O/C nanosheets were prepared using $Ni(Ac)_2$, $Mn(Ac)_2$ and $Co(Ac)_2$ as metal precursors, citric acid as complexing agent and glucose as the carbon source. Binary Ni–Co/C and Mn–O/C and single Co–O/C were also prepared for comparisons. The electrochemical properties of these materials were tested as electrode materials for supercapacitors and the ternary Mn–Ni–Co–O/C presented improved electrochemical performance.

2 Experimental

2.1 Materials Synthesis

The carbon coated ternary Mn–Ni–Co oxide was prepared by adapting the strategy reported by Fu *et al.* [25] and modifying the citrate sol-gel method reported in our previous study [27]. Analytical grade cobaltous acetate, manganese acetate, nickel acetate, citric acid, sodium chloride and glucose were used for the synthesis. In a typical synthetic procedure, a mixture of 0.245 g of manganese(II) acetate tetrahydrate ($Mn(Ac)_2{\cdot}4H_2O$), 0.249 g of nickel(II) acetate tetrahydrate ($Ni(Ac)_2{\cdot}4H_2O$), 0.996 g of cobalt(II) acetate tetrahydrate ($Co(Ac)_2{\cdot}4H_2O$), and 1.89 g of citric acid monohydrate ($C_6H_8O_7{\cdot}H_2O$) were dissolved in 50 mL of deionized water and the pH was adjusted to 7 by adding ammonia solution (25 %) dropwise. Then 16 g of NaCl and 3.6 g of glucose ($C_6H_{12}O_6$) were ground for 30 min with an agate mortar-pestle set and were then added to the solution mixture of $Ni(Ac)_2$, $Mn(Ac)_2$, $Co(Ac)_2$, and citric acid by stirring for 30 minutes. The mixture was dried at 60 °C for 10 h and then pyrolyzed at 750 °C for 6 h under N_2 atmosphere. The obtained black powder was heated again at 300 °C for 4 h in air to get the final crystalline phase ($Mn_{0.5}N_{0.5}Co_2O_4$/C), a puffy product. It was then cooled down to room temperature and washed with water and absolute alcohol several times to remove the NaCl, and then dried at 60 °C overnight in an oven.

The Co_3O_4/C, $MnCo_2O_4$/C and $NiCo_2O_4$/C samples were also prepared by following the same procedure except taking either the Mn or Ni acetate and Co acetate salts or only Co acetate. For comparison purposes, pure $Mn_{0.5}N_{0.5}Co_2O_4$ was prepared by further calcining the $Mn_{0.5}N_{0.5}Co_2O_4$/C sample at 600 °C for 6 h in air.

2.2 Characterizations

The crystal structure was investigated by using a Bruker D2 diffractometer (Co Kα radiation, $\lambda = 1.78060$ Å) at a scanning rate of $0.02° s^{-1}$ in a 2θ range from 10° to 90°. TEM and SEM images and the composition of the materials were obtained on FEI Nova Nano SEM 450 Scanning Electron Microscope with EDX attached to it and JEOL 2100 Transmission Electron Microscopy. Raman spectra were acquired on a Thermo Scientific DXR2 Smart Raman equipped with a 532 nm laser source at room temperature. The BET surface area was measured by N2 adsorption/desorption using an ASAP 2020 (Micrometrics instrument, USA) surface area analyzer and the pore size distribution was evaluated by using the Barrett-Joyner-Halenda (BJH) model.

2.3 Electrochemical Measurements

The electrochemical measurements were tested using a three-electrode configuration in 2 M KOH on a Gamry interface 1000 potentiostat/galvanostat. The Ag/AgCl electrode was used as a reference electrode and platinum wire was employed as a counter electrode. Cyclic voltammetry (CV) tests were performed between 0 and 0.6 V at various scan rates ranging from 5 to 100 $mV s^{-1}$. The galvanostatic GCD tests were conducted between 0 and 0.6 V at various current densities between 1 and

10 A g^{-1}. The electrochemical impedance spectroscopy (EIS) measurements were performed by applying an alternating current voltage with an amplitude of 5 mV in the frequency range of 0.1 Hz–100 kHz in the open circuit potential. The working electrode was prepared by using Nickel foam as a substrate and mixing 80 % active material, 10 % conductive carbon, and 10 % PVDF binder using a mortar and pestle and adding few drops of N-methyl pyrrolidone (NMP) to make a homogenous paste. The paste was then coated on to a 1 cm × 1 cm Nickel foam substrate, pressed and dried at 80 °C for 6 hours.

3 Results and Discussion

3.1 Structure and Morphology

As described in the experimental section, the MnNiCo–O/C was synthesized by the simple calcination of the mixture of metal acetates-citrate complex, glucose and NaCl. In this study, NaCl particle surface was employed as the template for the nanosheets as it has a face-centered cubic crystal structure [35,36] and citric acid was used as a chelating agent for the metal ions [37]. The high temperature pyrolysis under N_2 followed by calcination at low temperature in air results in the formation of ternary MnNiCo–O/C hybrid nanostructure due to the thermal carbonization of glucose and oxidation of metal citrates. The NaCl plays an essential role in synthesis process by assisting the formation of nanosheet structure, which agrees with other recent reports [38,39].

The XRD pattern of the prepared $Mn_{0.5}Ni_{0.5}Co_2O_4$/C is shown in Figure 1. It can be seen that the sample shows (111), (220), (311), (400), (422), (511), and (440) reflections, characteristic of the cubic phase spinel structure (space group *Fd3 m* (227), JCPDS No. 23-1237). A peak appears at $2\Theta = 30.5°$ (*d-spacing = 0.338 nm*), which corresponds to the diffraction peak of (002) crystallographic plane of graphite (JCPDS 65-6212). This indicates that after the carbonization, the carbon remained unaffected during annealing in air. These experimental data confirm the successful formation of MnNiCo–O/C hybrid after thermal treatment at 300 °C in air. Only the cubic phase $Mn_{0.5}Ni_{0.5}Co_2O_4$ and graphite is shown in the XRD pattern after calcinations in air. Likewise, similar XRD patterns were obtained for the other samples (Figure S2) except that NiO phase appeared in the $NiCo_2O_4$/C sample, which is consistent with our previous report [34].

The morphology of the $Mn_{0.5}Ni_{0.5}Co_2O_4$/C is shown in the SEM image in Figure 2(a). show the SEM images of $Mn_{0.5}Ni_{0.5}Co_2O_4$/C with a porous sheet like structure, which is more clearly shown in the TEM images. The elemental mapping and EDS of $Mn_{0.5}Ni_{0.5}Co_2O_4$/C (Figure 2(b) and (c)) confirm the presence of the elements Mn, Ni, Co, and O only and are homogenously distributed in the carbon matrix. TEM, HRTEM, and the corresponding SAED of $Mn_{0.5}Ni_{0.5}Co_2O_4$/C are shown in Figure 3. Fig 3(a) and (b) show the sheet like structure of carbon and the metal oxide nanoparticles are seen to be well-dispersed. In the highly magnified TEM image (Figure 3b), the carbon nanosheets seem transparent, suggesting the formation a porous, thin layer of sheet and the

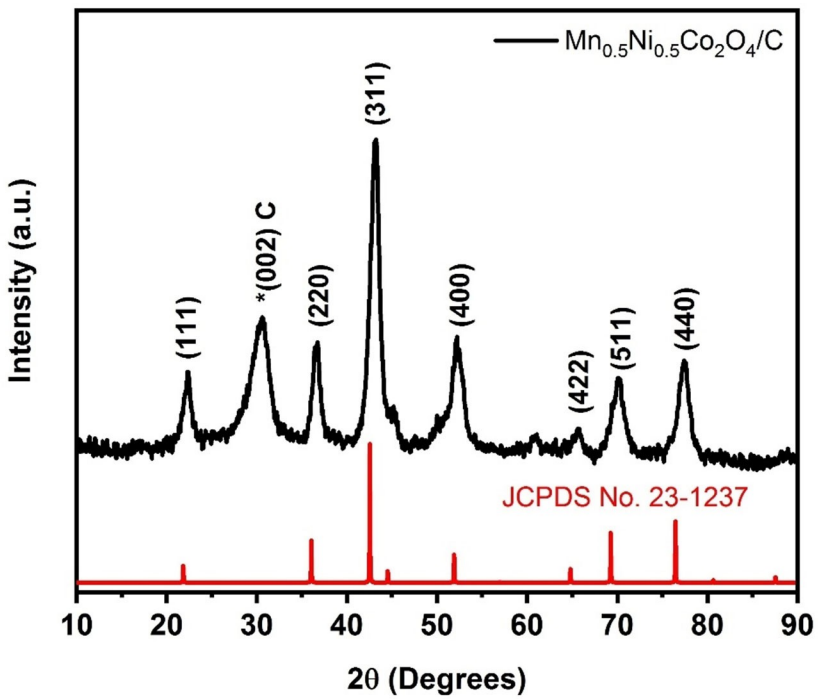

Fig. 1. XRD pattern of the $Mn_{0.5}Ni_{0.5}Co_2O_4$/C.

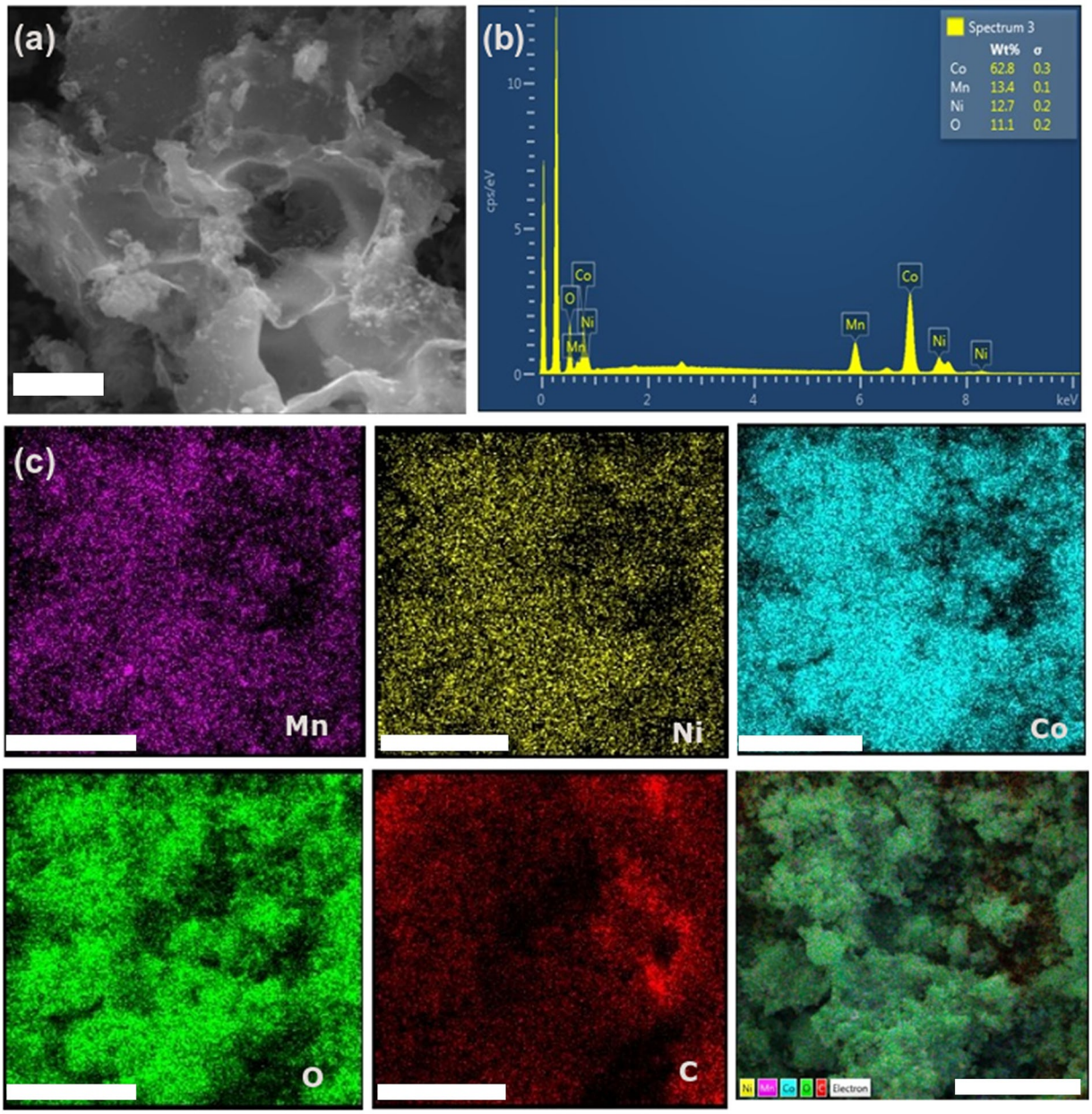

Fig. 2. (a) SEM image (**scale bar; 10 µm**), (b) EDS and (c) elemental mapping of $Mn_{0.5}Ni_{0.5}Co_2O_4$/C (**scale bar; 25 µm**). The Y and X axis labels are 'cps/eV and keV' respectively on (b)

metal oxide nanoparticles are dispersed over the carbon nanosheet. This is more clearly shown in Figure 3(d) where the thickness of the carbon layer is measured to be around 6 nm and it is shown to encapsulate the metal oxide nanoparticle well. The HRTEM and SAED in Figure 3(c) suggest the polycrystalline nature of the hybrid nanostructure. The HRTEM fringes of the $Mn_{0.5}Ni_{0.5}Co_2O_4$ crystal can be clearly seen and have a spacing of 0.246 nm, as denoted in Figure 3(c), corresponding to the spacing of (311) plane of $Mn_{0.5}Ni_{0.5}Co_2O_4$.

The Raman spectrum in Figure 4(a) shows the typical D and G bands of graphite for the $Mn_{0.5}Ni_{0.5}Co_2O_4$/C nanosheet at about 1,343 and 1,581 cm^{-1}, respectively. The ratio of peak intensity between the D and G bands (I_D/I_G) gives a suggestion of the degree of graphitization of carbon materials [40,41]. The calculated I_D/I_G ratio for the $Mn_{0.5}Ni_{0.5}Co_2O_4$/C is 1, suggesting that the carbon has some amorphous characteristics. Moreover, the presence of the characteristic peaks for the Mn–O, Ni–O and Co–O bonds below 800 cm^{-1} also confirms that high-quality $Mn_{0.5}Ni_{0.5}Co_2O_4$ spinel has been successfully synthesized [30]. The formation of the spinel oxides is further confirmed by the FTIR spectra (Figure S3), where the two characteristic absorption bands of metal-oxygen vibrations are observed at 655 and 574 cm^{-1} [42]. The carbon content in the hybrid nanostructure is determined

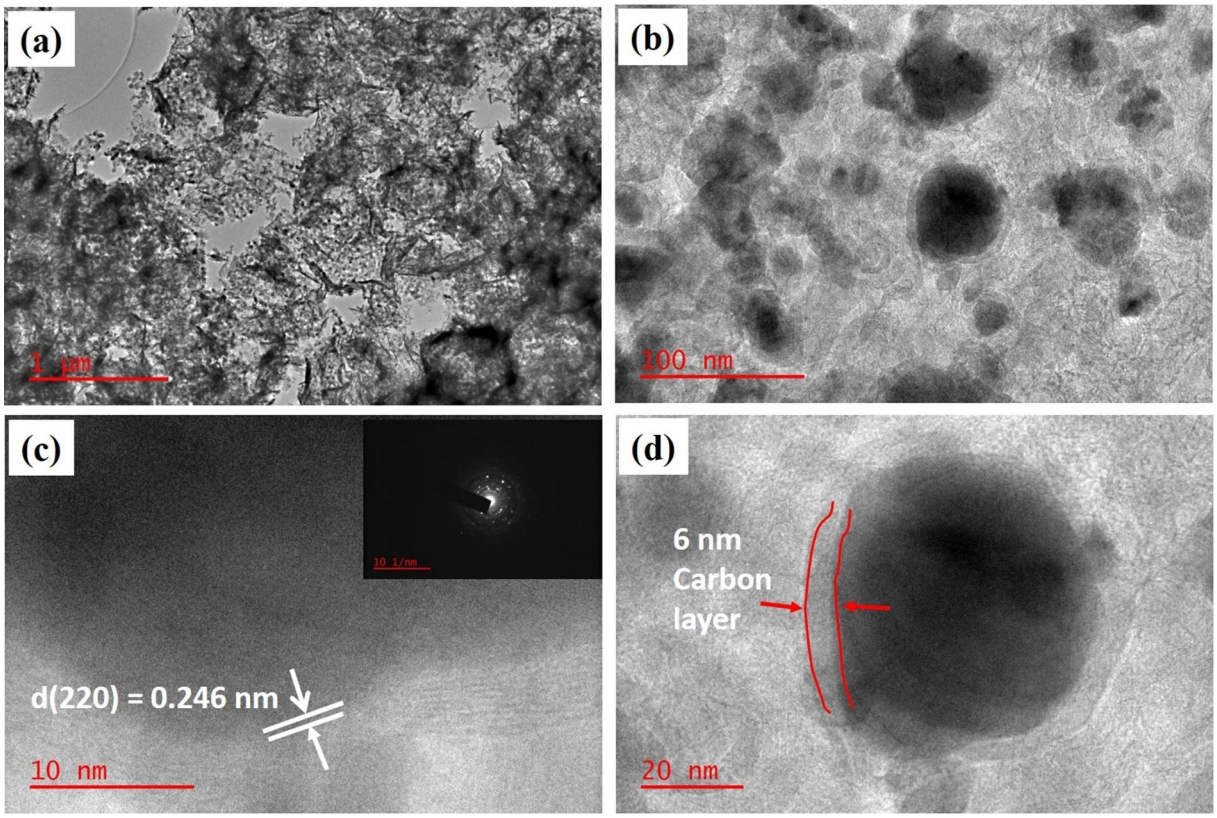

Fig. 3. (a and b) TEM image of $Mn_{0.5}Ni_{0.5}Co_2O_4$/C nanosheets at different magnifications; (c) HRTEM image of $Mn_{0.5}Ni_{0.5}Co_2O_4$/C nanosheets and the inset is the SAED; and (d) High magnification TEM image showing the carbon coating layer.

by TGA and is shown in Figure 4(b). The thermogravimetric curve of the $Mn_{0.5}Ni_{0.5}Co_2O_4$/C sample shows two main stages of weight loss. The first starts at 209 °C with a weight loss of about 21 %, and the second step between 397 and 620 °C has a weight loss of about 28 % and becomes stable up to 700 °C.

So, the total weight loss of about 51 % is related to the complete combustion of carbon. The carbon content of $Mn_{0.5}Ni_{0.5}Co_2O_4$/C composite is therefore 51 % and the remaining 49 % is the ternary $Mn_{0.5}Ni_{0.5}Co_2O_4$ oxide.

Figure 4(c) & (d) show the nitrogen adsorption/desorption isotherms and pore size distributions of the $Mn_{0.5}Ni_{0.5}Co_2O_4$/C composite, respectively. The nitrogen adsorption/desorption isotherms are observed to be a typical type IV with a hysteresis loop in the relative pressure range of 0.35–0.95, indicating a mesoporous structure and a narrow mesopore size distribution. The pore size distribution is shown in Figure 4(d) exhibits a multi-modal pore size distribution, with peaks at 2.7 nm, 9 nm, and a broad peak at approximately 37.8 nm. The average pore diameter is about 10.9 nm based on Barrett-Joyner-Halenda (BJH) adsorption. The BET specific surface area is measured to be 264.7 $m^2 g^{-1}$. These results particularly characterize the porous structure of the graphite carbon sheets. Such a pore structure could be advantageous for supercapacitors because of the high surface area, multi-modal pore size distribution, and a large pore volume. This can make the diffusion of electrolyte and charge transfer easier [43]. The larger surface area of the $Mn_{0.5}Ni_{0.5}Co_2O_4$/C composite, compared to the other materials (Table S1) is an interesting result and needs further investigation. Although the reason for the larger surface area is unknown at this time, it may be due to the ternary metal nano-composite forming more porous and variable sheet-like structures when compared to the other materials.

3.2 Electrochemical Properties

Cyclic voltammograms (CV) were measured to explore the potential application of the synthesized samples as electrode materials for supercapacitors. Figure 5(a) shows the cyclic voltammogram curves of Co_3O_4/C, $MnCo_2O_4$/C, $NiCo_2O_4$/C and $Mn_{0.5}Ni_{0.5}Co_2O_4$/C at a scan rate of 5 $mV s^{-1}$ in 2 M KOH in the potential window of 0–0.6 V.

The shapes of the curves clearly show well-defined redox peaks within the potential range indicating the battery-like behavior of the materials owing to the faradic redox reactions. The faradic reactions taking place within the electrode material corresponding to the reversible redox reactions are related to M–O/M–O–OH (M = Co, Ni, and Mn) [20,44,45]. The redox reactions involved in the electrochemical process can be described as [27];

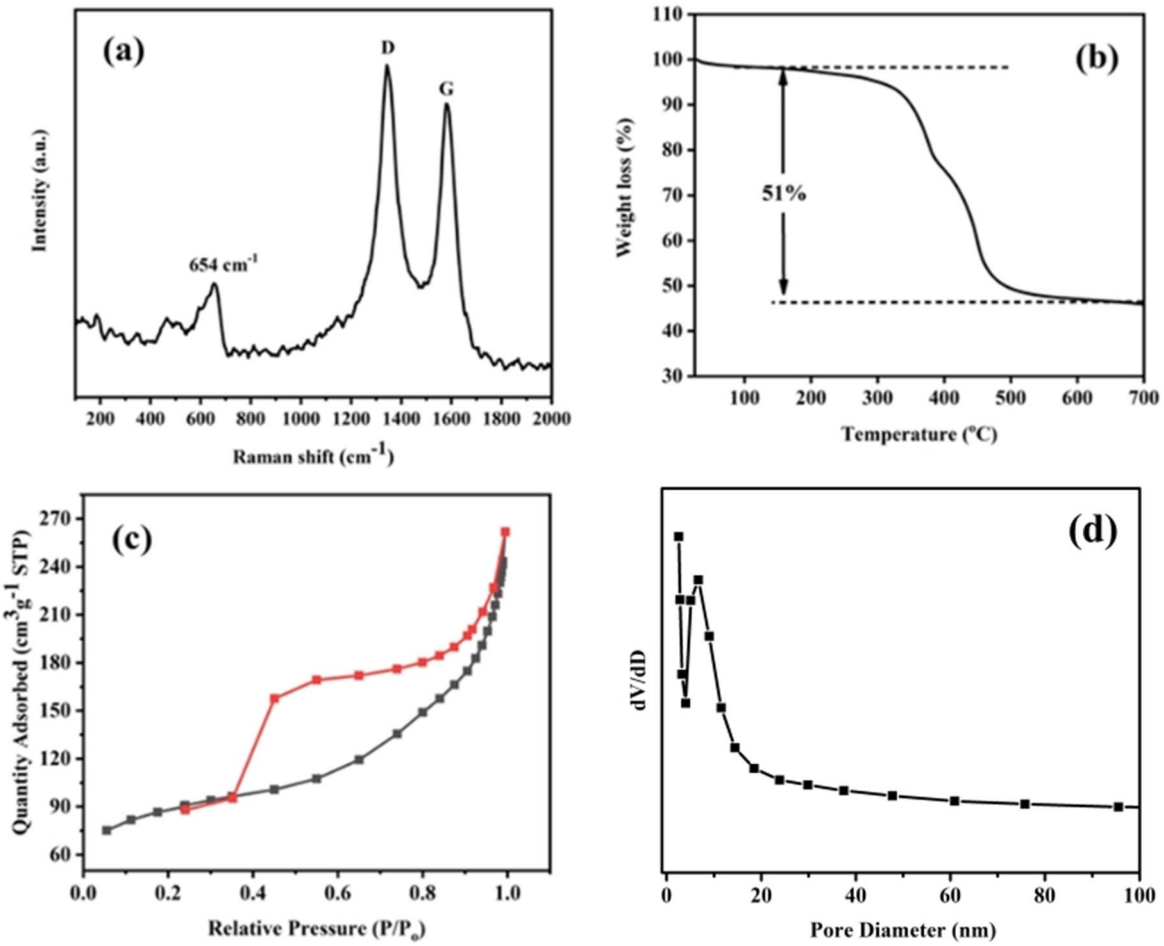

Fig. 4. Raman spectrum (a) TGA profile (b) Nitrogen adsorption/desorption isotherms (c) and (d) pore size distributions of the $Mn_{0.5}Ni_{0.5}Co_2O_4$/C.

$$(Mn,\ Ni)Co_2O_4 + OH^- + H_2O \leftrightarrow (Mn,\ Ni)OOH + 2CoOOH + 2e^- \quad (1)$$

$$MOOH + OH^- \leftrightarrow MO_2 + H_2O + e^- \quad (2)$$

where M represents Co or Ni and Mn. The area of the CV curves for the $Mn_{0.5}Ni_{0.5}Co_2O_4$/C samples were larger than Co_3O_4/C, $NiCo_2O_4$/C, and $MnCo_2O_4$/C, indicating the highest capacity of the $Mn_{0.5}Ni_{0.5}Co_2O_4$/C materials. Moreover, the redox peaks of the electrode materials shift moving from single to ternary metal oxides.

The specific capacity (C_s, mAh g^{-1}) from CV is calculated using the equation [46]:

$$C_s = \frac{\oint IdV}{3.6\ mS} \quad (3)$$

where $\oint$ IdV is the voltammetric charge, which is an area under the curve of the CV, I (A) is the discharging current, m (g) is the active mass of the electrodes, and S (V s^{-1}) is the scan rate. The specific capacity of Co_3O_4/C, $NiCo_2O_4$/C, $MnCo_2O_4$/C, and $Mn_{0.5}Ni_{0.5}Co_2O_4$/C electrodes are 41.6, 53.8, 67.8, and 96.5 mAh g^{-1} at a scan rate of 5 mV s^{-1}, respectively. The ternary $Mn_{0.5}Ni_{0.5}Co_2O_4$/C hybrid electrode exhibits enhanced specific capacity compared to the mono and binary metal oxide-based materials. The higher Cs value of the ternary $Mn_{0.5}Ni_{0.5}Co_2O_4$/C hybrid electrode systems can be attributed to the synergistic effect of the rich redox reaction of the multicomponent metals and the high surface area and enhanced conductivity brought about by the carbon nanosheets. With the increase in the scan rate, the redox peaks in CV curves keeps increasing suggesting the typical electrochemical signature of transition metal oxide-based battery-type materials (Figure 5(b)). Similar results were reported earlier emphasizing the synergetic effect of multicomponent systems in mixed metal oxides [27,47]. The carbon nanosheet in the hybrid nanostructure serves as a conductive matrix supporting the metal oxide and providing large surface area, fully utilizing the electrochemical performance of the ternary metal oxide.

The performance of supercapacitors for practical applications is mainly determined by their charge-discharge features. Galvanostatic charge-discharge experiments of the samples were measured to further explore their potential application. The specific capacity of the

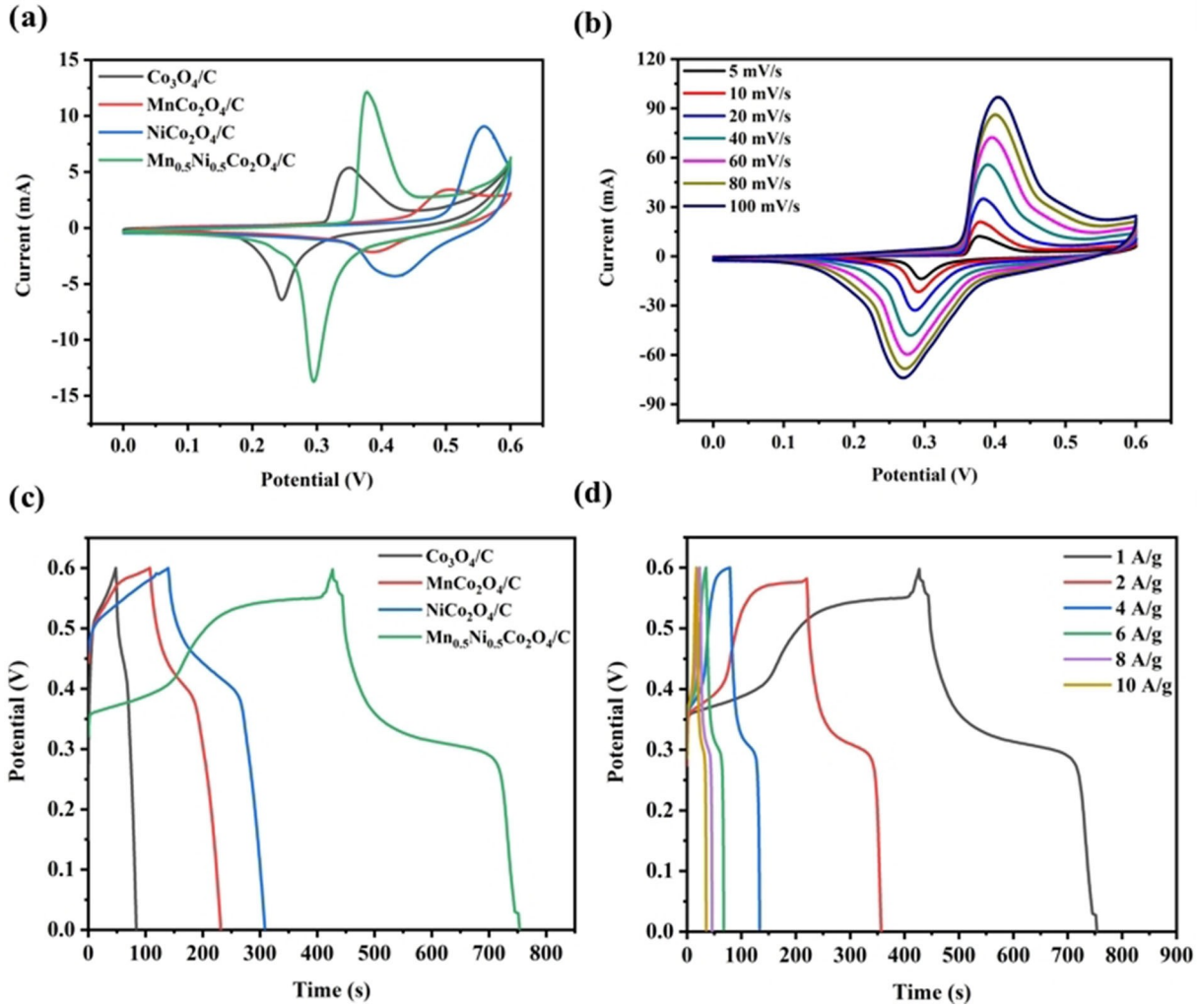

Fig. 5. (a) CV curves of Co_3O_4/C, $MnCo_2O_4$/C, $NiCo_2O_4$/C and $Mn_{0.5}Ni_{0.5}Co_2O_4$/C at a scan rate of 5 mV s^{-1} (b) CV curves of $Mn_{0.5}Ni_{0.5}Co_2O_4$/C at varying scan rates from 5–100 mV s^{-1} (c) GCD curves of Co_3O_4/C, $MnCo_2O_4$/C, $NiCo_2O_4$/C and $Mn_{0.5}Ni_{0.5}Co_2O_4$/C at 1 A g^{-1} and (d) GCD curves of $Mn_{0.5}Ni_{0.5}Co_2O_4$/C at different current density at 1, 2, 4, 6, 8 and 10 A g^{-1}.

electrode calculated from the charge-discharge curves is obtained from the three electrodes testing using the following relation [46,48]:

$$C_s = \frac{I\Delta t}{3.6\ m} \quad (4)$$

where I is the current (A), Δt represents the discharging time (s) and m is the mass of the active material (g). Figure 5(c) displays the galvanostatic charge-discharge profiles of the electrode materials at a current density of 1 A g^{-1}. The ternary $Mn_{0.5}Ni_{0.5}Co_2O_4$/C shows more distinct voltage plateaus compared to the other samples and are consistent with the redox peaks observed in the CV curves. From the discharge times, we can see that the $Mn_{0.5}Ni_{0.5}Co_2O_4$/C samples exhibited higher capacitance than Co_3O_4/C, $NiCo_2O_4$/C, and $MnCo_2O_4$/C. The calculated capacitance of 10.1, 34.3, 46.5, and 91.2 mAh g^{-1} for Co_3O_4/C, $NiCo_2O_4$/C, and $MnCo_2O_4$/C and $Mn_{0.5}Ni_{0.5}Co_2O_4$/C, respectively, further implies the potential of $Mn_{0.5}Ni_{0.5}Co_2O_4$/C as electrode materials for supercapacitors. The $Mn_{0.5}Ni_{0.5}Co_2O_4$/C electrode exhibits the highest capacitance, consistent with the results from CV and charge/discharge curves. The galvanostatic charge-discharge curves of the $Mn_{0.5}Ni_{0.5}Co_2O_4$/C electrode materials recorded at higher current densities ranging from 2 A g^{-1} to 10 A g^{-1} to estimate the rate performance were shown in Figure 5(d). Interestingly, 60 % of the capacity for $Mn_{0.5}Ni_{0.5}Co_2O_4$/C is retained from 1 A g^{-1} to 6 A g^{-1} (Figure 6(a)). The above electrochemical measurements demonstrate the interesting battery-like behavior of the $Mn_{0.5}Ni_{0.5}Co_2O_4$/C samples, in terms of their specific capacity and rate capability. The galvanostatic charge-discharge experiments for a bare $Mn_{0.5}Ni_{0.5}Co_2O_4$ without the carbon nanosheet support and $Mn_{0.5}Ni_{0.5}Co_2O_4$/C were done at 1 A g^{-1} for comparison (Figure S6). It has clearly demonstrated the enhancement in capacity for $Mn_{0.5}Ni_{0.5}Co_2O_4$/C with a higher discharge time than the

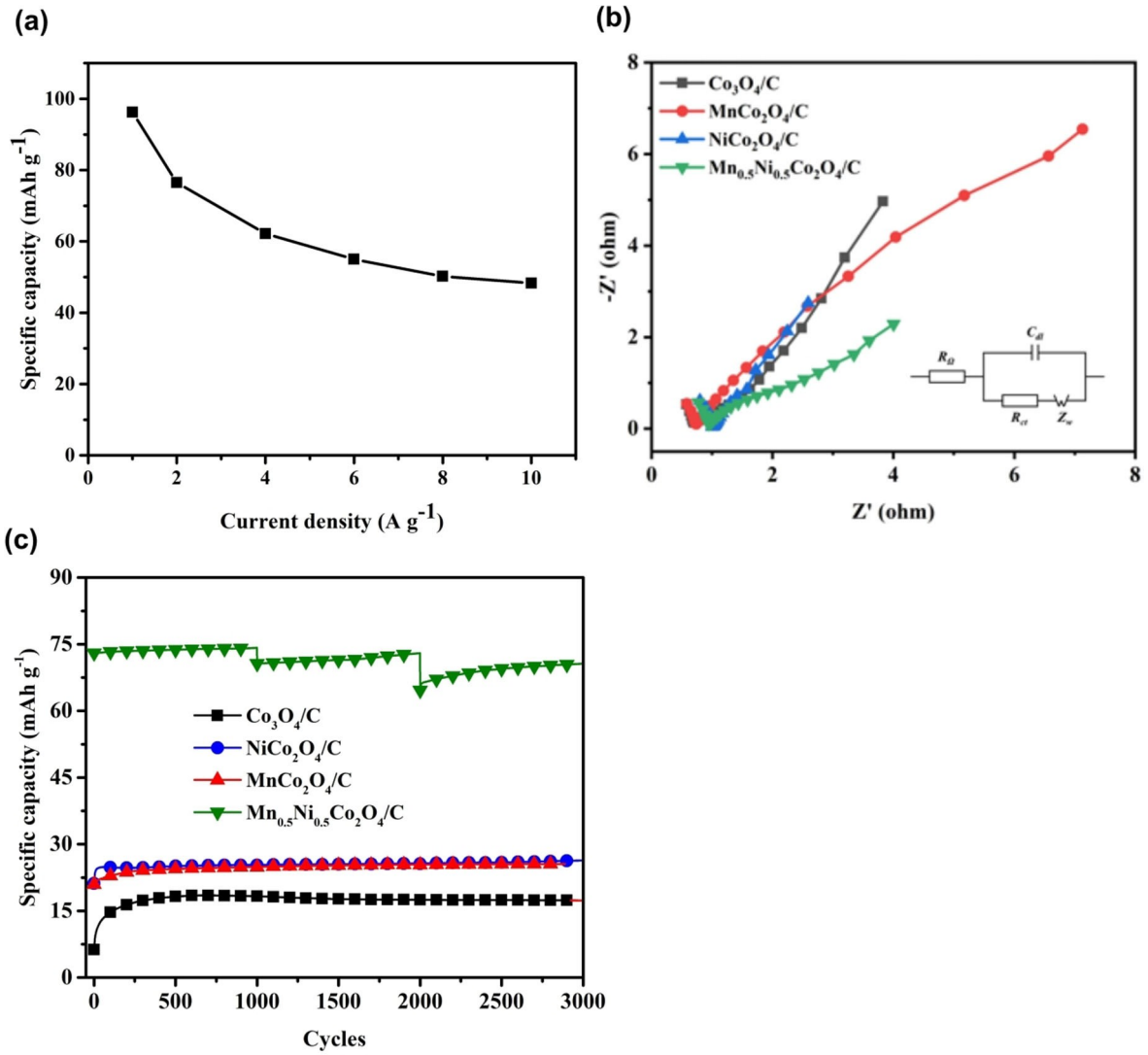

Fig. 6. (a) Specific capacity of $Mn_{0.5}Ni_{0.5}Co_2O_4$/C at different current densities (b) EIS measured at the open circuit potential in the frequency range from 0.1 to 100 kHz for Co_3O_4/C, $NiCo_2O_4$/C, and $MnCo_2O_4$/C and $Mn_{0.5}Ni_{0.5}Co_2O_4$/C. Inset shows the modeled equivalent circuit (c) Cycling performances during 3,000 cycles at a current density of 6 A g^{-1} for Co_3O_4/C, $NiCo_2O_4$/C, and $MnCo_2O_4$/C and $Mn_{0.5}Ni_{0.5}Co_2O_4$/C.

bare ternary metal oxide due to the carbon support. The $Mn_{0.5}Ni_{0.5}Co_2O_4$/C electrode exhibited comparable electrochemical performance to some of the previously reported mixed transition metal oxides and those supported on carbon materials and is shown in Table 1. The following reasons can be attributed to the high capacity of the ternary metal oxide-based electrodes. First, the high surface area of the composite electrode is beneficial for ion/electron transfer in the electrode. Secondly, the synergistic effect of multicomponent metals facilitates fast ion/electron transfer.

Electrochemical impedance spectroscopy (EIS) measurements were performed to obtain more information on the resistance of the electrodes. The Nyquist plots given

Table 1. Comparison of the electrochemical properties of the $Mn_{0.5}Ni_{0.5}Co_2O_4$/C nanosheets with some previously reported mixed transition metal oxides-based electrode materials.

Active Materials	Specific Capacitance	Cycling stability	Ref.
Porous NiCoMn ternary metal oxide/graphene nanocomposites	115mAh g^{-1} at 1 A g^{-1}	96 % (2000 cycles)	[30]
Bundle-like $CuCo_2O_4$ microstructures	303 C g^{-1} at 1 A g^{-1}	69.77 % (5000 cycles)	[51]
Ternary $Mn_{0.5}Ni_{0.5}Co_2O_4$/C	91.2 mAh g^{-1} (325 C g^{-1}) at 1 A g^{-1}	96.4 % (3000 cycles)	This work

in Figure 6(b) show the evident straight lines in the low frequency range for all the electrodes. The corresponding fitted equivalent circuit is also presented in the inset. The intercept of the semicircle with the real axis at high frequencies represents the equivalent series resistance (ESR) [49]. In general, supercapacitors reveal resistive behavior at high frequencies and capacitive behavior at low frequencies [50]. The ternary metal oxide shows smaller resistance, indicating high conductivity. The equivalent series resistance is 1.0, 0.94, 0.71, and 0.57 Ohm for Co_3O_4/C, $NiCo_2O_4$/C, $MnCo_2O_4$/C and $Mn_{0.5}Ni_{0.5}Co_2O_4$/C, respectively demonstrating the benefit of the ternary mixed metal oxides.

Long term cycling stability is an important criterion for evaluating the performance metal oxide-based supercapacitor electrodes for practical applications. The cycling stability of Co_3O_4/C, $NiCo_2O_4$/C, $MnCo_2O_4$/C and $Mn_{0.5}Ni_{0.5}Co_2O_4$/C samples were executed at 6 A/g using charge/discharge test over 3000 cycles. Figure 6(c) shows the specific capacity of the electrodes as a function of cycle number during galvanostatic charge/discharge test over 3000 cycles at a current density of $6\,A\,g^{-1}$. $Mn_{0.5}Ni_{0.5}Co_2O_4$/C sample shows the best cyclic stability with specific capacity of $74.6\,mAh\,g^{-1}$ after 3000 cycles and 96.4 % capacity retention compared to the binary and single transition metal oxides indicating the superior performance of ternary systems.

4 Conclusions

In summary, carbon encapsulated Co_3O_4/C, $MnCo_2O_4$/C, $NiCo_2O_4$/C and $Mn_{0.5}Ni_{0.5}Co_2O_4$/C nanosheets were successfully prepared by a facile and scalable method by modifying the citric acid assisted sol-gel method and employing a NaCl template-directed pyrolysis and glucose as a carbon source. The prepared ternary $Mn_{0.5}Ni_{0.5}Co_2O_4$/C nanosheets exhibit higher electrochemical performance as electrode materials for supercapacitors compared to the binary $MnCo_2O_4$/C and $NiCo_2O_4$/C and single metal Co_3O_4/C electrodes. The porous structure and large surface area of the $Mn_{0.5}Ni_{0.5}Co_2O_4$/C electrode provided by the carbon sheets and the synergistic effect of the multimetal components results in an enhanced electrochemical performance. The $Mn_{0.5}Ni_{0.5}Co_2O_4$/C electrode exhibit a specific capacity of $91.2\,mAh\,g^{-1}$ at a current density of $1\,A\,g^{-1}$. It also delivers a specific capacity of $74.6\,mAh\,g^{-1}$ after 3000 cycles at a current density of $6\,A\,g^{-1}$ with relatively high capacity retention of 96.4 %. Therefore, the good electrochemical properties combined with the facile preparation method will make it an attractive electrode material for promising application in high performance supercapacitors.

Acknowledgements

The work reported herein was partially funded by the National Research Foundation (South Africa). In addition, the authors thank the Centre for Nanomaterials Science Research at the Department of Chemical Sciences, University of Johannesburg, and the School of Chemistry at University of the Witwatersrand, for support and access to research facilities.

Data Availability Statement

The data that support the findings of this study are available from the corresponding author upon reasonable request.

References

[1] G. Wang, L. Zhang, J. Zhang, *Chem. Soc. Rev.* **2012**, *41*, 797–828.
[2] B. C. Melot, J.-M. Tarascon, *Acc. Chem. Res.* **2013**, *46*, 1226–1238.
[3] P. Simon, Y. Gogotsi, B. Dunn, *Science.* **2014**, *343*, 1210–1211.
[4] N. Choi, Z. Chen, S. A. Freunberger, X. Ji, Y. Sun, K. Amine, G. Yushin, L. F. Nazar, J. Cho, P. G. Bruce, *Angew. Chem. Int. Ed.* **2012**, *51*, 9994–10024; *Angew. Chem.* **2012**, *124*, 10134–10166.
[5] J. P. Barton, D. G. Infield, *IEEE Trans. Ener. Conv.* **2004**, *19*, 441–448.
[6] S. Ntanos, M. Skordoulis, G. Kyriakopoulos, G. Arabatzis, M. Chalikias, S. Galatsidas, A. Batzios, A. Katsarou, *Sustainability.* **2018**, *10*, 2626.
[7] I. Hadjipaschalis, A. Poullikkas, V. Efthimiou, *Renewable Sustainable Energy Rev.* **2009**, *13*, 1513–1522.
[8] J. Xie, P. Yang, Y. Wang, T. Qi, Y. Lei, C. M. Li, *J. Power Sources* **2018**, *401*, 213–223.
[9] M. Winter, R. J. Brodd, *Chem. Rev.* **2004**, *104*, 10, 4245–4270.
[10] T. S. Mathis, N. Kurra, X. Wang, D. Pinto, P. Simon, Y. Gogotsi, *Adv. Energy Mater.* **2019**, *9*, 1902007.
[11] Z. Yu, L. Tetard, L. Zhai, J. Thomas, *Energy Environ. Sci.* **2015**, *8*, 702–730.
[12] M. R. Lukatskaya, B. Dunn, Y. Gogotsi, *Nat. Commun.* **2016**, *7*, 1–13.
[13] F. Yu, T. Huang, P. Zhang, Y. Tao, F.-Z. Cui, Q. Xie, S. Yao, F. Wang, *Energy Storage Mater.* **2019**, *22*, 235–255.
[14] C. Young, T. Park, J. W. Yi, J. Kim, M. S. A. Hossain, Y. V. Kaneti, Y. Yamauchi, *ChemSusChem.* **2018**, *11*, 3546–3558.
[15] Y.-Y. Huang, L.-Y. Lin, *ACS Appl. Energy Mater.* **2018**, *1*, 2979–2990.
[16] G. A. Snook, P. Kao, A. S. Best, *J. Power Sources* **2011**, *196*, 1–12.
[17] H. Liu, X. Liu, S. Wang, H.-K. Liu, L. Li, A review, *Energy Storage Mater.* **2020**, *28*, 122–145.
[18] C. Yuan, H. B. Wu, Y. Xie, X. W. Lou, *Angew. Chem. Int. Ed.* **2014**, *53*, 1488–1504; *Angew. Chem.* **2014**, *126*, 1512–1530.
[19] A. Y. Faid, H. Ismail, *Materials Today Energy.* **2019**, *13*, 285–292.
[20] I. Hussain, S. G. Mohamed, A. Ali, N. Abbas, S. M. Ammar, W. Al Zoubi, Journal of *Electroanal. Chem.* **2019**, *837*, 39–47.
[21] H. J. Lee, J. H. Lee, S. Chung, J. W. Choi, *Angew. Chem. Int. Ed.* **2016**, *55*, 3958–3962; *Angew. Chem.* **2016**, *128*, 4026–4030.
[22] A. Pendashteh, J. Palma, M. Anderson, R. Marcilla, *RSC Adv.* **2016**, *6*, 28970–28980.

[23] C. Mariappan, S. Upadhyay, V. Kumar, S. Indris, H. Ehrenberg, *Ceram. Int.* **2018**, *44*, 8864–8869.
[24] L. Li, Y. Zhang, F. Shi, Y. Zhang, J. Zhang, C. Gu, X. Wang, J. Tu, *ACS Appl. Mater. Interfaces* **2014**, *6*, 18040–18047.
[25] J. Zhao, M. Li, J. Li, C. Wei, Y. He, Y. Huang, Q. Li, *Appl. Surf. Sci.* **2017**, *425*, 1158–1167.
[26] J.-M. Luo, B. Gao, X.-G. Zhang, *Mater. Res. Bull.* **2008**, *43*, 1119–1125.
[27] M. S. Tamboli, D. P. Dubal, S. S. Patil, A. F. Shaikh, V. G. Deonikar, M. V. Kulkarni, N. N. Maldar, A. M. Asiri, P. Gomez-Romero, B. B. Kale, *Chem. Eng. J.* **2017**, *307*, 300–310.
[28] L. L. Zhang, X. Zhao, *Chem. Soc. Rev.* **2009**, *38*, 2520–2531.
[29] H. Zhang, D. Xiao, Q. Li, Y. Ma, S. Yuan, L. Xie, C. Chen, C. Lu, *J. Energy Chem.* **2018**, *27*, 195–202.
[30] J. S. Sanchez, A. Pendashteh, J. Palma, M. Anderson, R. Marcilla, *Electrochim. Acta* **2018**, *279*, 44–56.
[31] F. Ochai-Ejeh, M. J. Madito, K. Makgopa, M. N. Rantho, O. Olaniyan, N. Manyala, *Electrochim. Acta* **2018**, *289*, 363–375.
[32] G. Fu, Z. Liu, J. Zhang, J. Wu, L. Xu, D. Sun, J. Zhang, Y. Tang, P. Chen, Spinel, *Nano Research.* **2016**, *9*, 2110–2122.
[33] F. Wen, H. Hou, J. Xiang, X. Zhang, Z. Su, S. Yuan, Z. Liu, *Carbon.* **2015**, *89*, 372–377.
[34] T. H. Dolla, K. Pruessner, D. G. Billing, C. Sheppard, A. Prinsloo, E. Carleschi, B. Doyle, P. Ndungu, *J. Alloys Compd.* **2018**, *742*, 78–89.
[35] D. Chakraborty, G. Patey, *J. Phys. Chem. Lett.* **2013**, *4*, 573–578.
[36] D. Chakraborty, G. Patey, *Chem. Phys. Lett.* **2013**, *587*, 25–29.
[37] D. Soni, R. Pal, *Electroanalysis.* **2016**, *28*, 1951–1956.
[38] X. Leng, S. Wei, Z. Jiang, J. Lian, G. Wang, Q. Jiang, *Sci. Rep.* **2015**, *5*, 16629.
[39] J. Zhang, W. Ren, Y. Zhou, P. Li, L. Xu, D. Sun, P. Wu, Y. Zhou, Y. Tang, *Chem. - Eur. J.* **2016**, *22*, 9599–9606.
[40] C. He, S. Wu, N. Zhao, C. Shi, E. Liu, J. Li, *ACS Nano.* **2013**, *7*, 4459–4469.
[41] J. G. Kim, Y. Kim, Y. Noh, W. B. Kim, *ChemSusChem.* **2015**, *8*, 1752–1760.
[42] B. Lefez, P. Nkeng, J. Lopitaux, G. Poillerat, *Mater. Res. Bull.* **1996**, *31*, 1263–1267.
[43] J. Zhang, L.-B. Kong, J.-J. Cai, H. Li, Y.-C. Luo, L. Kang, *Microporous Mesoporous Mater.* **2010**, *132*, 154–162.
[44] A. N. Naveen, S. Selladurai, *Electrochim. Acta* **2014**, *125*, 404–414.
[45] F. Zhang, C. Yuan, X. Lu, L. Zhang, Q. Che, X. Zhang, *J. Power Sources* **2012**, *203*, 250–256.
[46] T. P. Mofokeng, A. K. Ipadeola, Z. N. Tetana, K. I. Ozoemena, *ACS Omega.* **2020**.
[47] C. Wu, J. Cai, Y. Zhu, K. Zhang, *ACS Appl. Mater. Interfaces.* **2017**, *9*, 19114–19123.
[48] L. Chen, Y. Jiao, Z. Li, Y. Gao, *Electrochim. Acta* **2019**, *299*, 388–394.
[49] Z. Fan, J. Yan, T. Wei, L. Zhi, G. Ning, T. Li, F. Wei, *Adv. Funct. Mater.* **2011**, *21*, 2366–2375.
[50] P. L. Taberna, P. Simon, J. F. Fauvarque, *J. Electrochem. Soc.* **2003**, *150*, A292.
[51] J. Sun, X. Du, R. Wu, Y. Zhang, C. Xu, H. Chen, *ACS Appl. Mater. Interfaces* **2020**, *3*, 8026–8037.

Received: September 10, 2020
Accepted: September 16, 2020
Published online on October 7, 2020

